Clutter Removal of Near-Field UWB SAR Imaging for Pipeline Penetrating Radar

Alireza Akbarpour, Somayyeh Chamaani, *Member, IEEE*, Juergen Sachs, and Giovanni Del Galdo, *Member, IEEE*

Abstract—Recently, ultrawideband (UWB) near-field synthetic aperture radar (SAR) imaging has been proposed for pipeline penetrating radar applications thanks to its capability in providing suitable resolution and penetration depth. Because of geometrical restrictions, there are many complicated sources of clutter in the pipe. However, this issue has not been investigated yet. In this article, we investigate some well-known clutter removal algorithms using full-wave simulated data and compare their results considering image quality, signal to clutter ratio and contrast. Among candidate algorithms, two-dimensional singular spectrum analysis (2-D SSA) shows a good potential to improve the signal to clutter ratio. However, basic 2-D SSA produces some artifacts in the image. Therefore, to mitigate this issue, we propose "modified 2-D SSA." After developing the suitable clutter removal algorithm, we propose a complete algorithm chain for pipeline imaging. An UWB near-field SAR monitoring system including an UWB M-sequence sensor and automatic positioner are implemented and the image of drilled perforations in a concrete pipe mimicking oil well structure as a case study is reconstructed to test the proposed algorithm. Compared to the literature, a comprehensive near-field SAR imaging algorithm including new clutter removal is proposed and its performance is verified by obtaining high-quality images in experimental results.

Index Terms—Clutter removal, imaging, near-field, pipeline penetrating radar, synthetic aperture radar (SAR), two-dimensional singular spectrum analysis (2-D SSA), ultrawideband (UWB).

I. Introduction

NOWADAYS, pipeline penetrating radars (PPR) has been considered for pipeline condition assessment in various areas such as water pipeline, asbestos cement pipeline in sewer pipeline, gas pipelines, etc. In these applications, the PPR is used for mapping the wall thickness, corrosion area, pipe wall fractures, and every anomaly within or outside of the pipe wall [1]–[7].

Recently, ultrawideband (UWB) near-field synthetic aperture radar (SAR) imaging as a PRP has found a new application in oil well monitoring [8]–[14]. The oil and gas companies take care to preserve functionality of oil well, extend its life time, and decrease maintenance cost by monitoring of oil well. To this aim, they regularly inspect oil well wall to prevent possible phenomena such as fracturing well wall, clogging drilled perforations in the well wall, and any anomaly in well wall. The perforations allow the oil flows from the natural reservoir into the well, and their condition in terms of opening, clogging, or partial clogging affect directly on the oil well efficiency [8]. Due to the complexity of the medium and imaging in the near-field, oil well monitoring like other pipeline monitoring applications faces various sources of clutter that must be reduced to monitor the perforations condition.

Several clutter reduction techniques have been applied for ground penetrating radar (GPR), through wall imaging (TWI), and near-field imaging in the literature [15], [16]–[25]. However, based on our knowledge, clutter removal problem for oil well monitoring and more generally pipeline monitoring has not been considered, yet.

The clutter removal techniques are classified as statistical signal processing, model-based methods, and classical filtering [22]. The main drawback of model-based methods is that their ability highly depends on how well the real scenario fits the assumed model. Therefore, we focus our attention on statistical signal processing and filtering methods.

According to the literature, the capability of these methods strongly depends on the environment and clutter source types. For example, in GPR and TWI, one clutter source is air ground and air wall interference, respectively; and in these cases, filtering methods have good performance for removing this interference if the surface is smooth and homogenous. The classical filtering method of mean subtraction is also a good candidate for Tx/Rx cross talk and extracting background signal. Another source is scattering from neighboring unevenly distributed objects in the scene. In this case, blind source separation methods, i.e., singular value decomposition (SVD) [19]; principal component analysis [23]; independent component analysis (ICA) [26]; matrix pencil method (MPM) [16]; and singular spectrum analysis (SSA) are usually used for separating their contribution [27]. However, in pipeline monitoring, the medium is more different and complex. In this case, many clutter sources including electromagnetic waves due to excitation of waveguide modes in broadband spectrum, scattering from whole interior surface of pipe, coupling between Tx/Rx antenna, radiation of guided/surface waves, and the presence of other objects near the

antenna such as sensor holder contribute in the received signal. Therefore, to remove the clutter in oil well monitoring, as a new medium, more complex algorithms or series of algorithms are required.

In this article, oil well monitoring as a new application in pipeline monitoring area are considered, and all simulations and measurements are done considering oil well geometry and conditions. First, to consider realistic clutter sources, an UWB near-field SAR imaging system for oil well structure is simulated in CST microwave studio (MWS) software. To address the clutter issue, we apply some candidate methods such as mean removal, L1norm subtraction (should not be confused with L1-norm minimization) [28], SVD, and two-dimensional SSA (2-D SSA) on raw data and evaluate their performance after image reconstruction by Global Back Projection method (GBP). Recently, 2-D SSA has been used in image processing for reducing noise and feature extraction [29], [30]. In [27], it was proposed for clutter removal. However, it needs further work to be applicable in radar imaging; because it only separated the raw data to some clusters and final image was not reconstructed to evaluate its performance, properly. Therefore, first, we investigate its performance; and due to observing some artifacts after applying basic 2-D SSA, we propose a complementary step for 2D-SSA to remove these artifacts. We call the complete algorithm "modified 2-D SSA." After preliminary investigation of the nominated methods, we propose a signal processing chain to reconstruct the image of perforations drilled in oil well wall. To verify its performance in a semi-real scenario, an experimental setup including a positioner, and an UWB M-sequence sensor is implemented for oil well monitoring.

Compared to [8]–[10], which did not consider the clutter issue, we examined many clutter removal algorithms and proposed the most effective of them with a signal processing chain to monitor pipeline easily. The results of applying the proposed method were an impressive improvement in the image of perforations. Thanks to proper signal processing algorithms, the signal to clutter ratio (SCR), contrast, and the quality of image were improved. In addition, against [8], [10] that used an expensive impulse generator and a sampling oscilloscope, we used a more affordable sensor which has simpler structure and better electrical performance.

In the rest of the article, first, we introduce oil well structure and clutter sources in this near-field SAR imaging scenario. In Section III, we describe some clutter removal techniques applied for imaging applications, and evaluate their performance using oil well simulated data in Section IV. Then, in Section V, an algorithm for oil well monitoring is proposed. In Section VI, the experimental setup including oil well positioner, and UWB sensor is described, and measurement results are illustrated. Finally, the conclusion of this article is presented in Section VII.

II. OIL WELL MONITORING

A. Oil Well Structure

Oil well structure is illustrated in Fig. 1(a). It is a deep borehole, where its depth varies from a few hundred meters to a few kilometers depending on the reservoir type. Size of hole
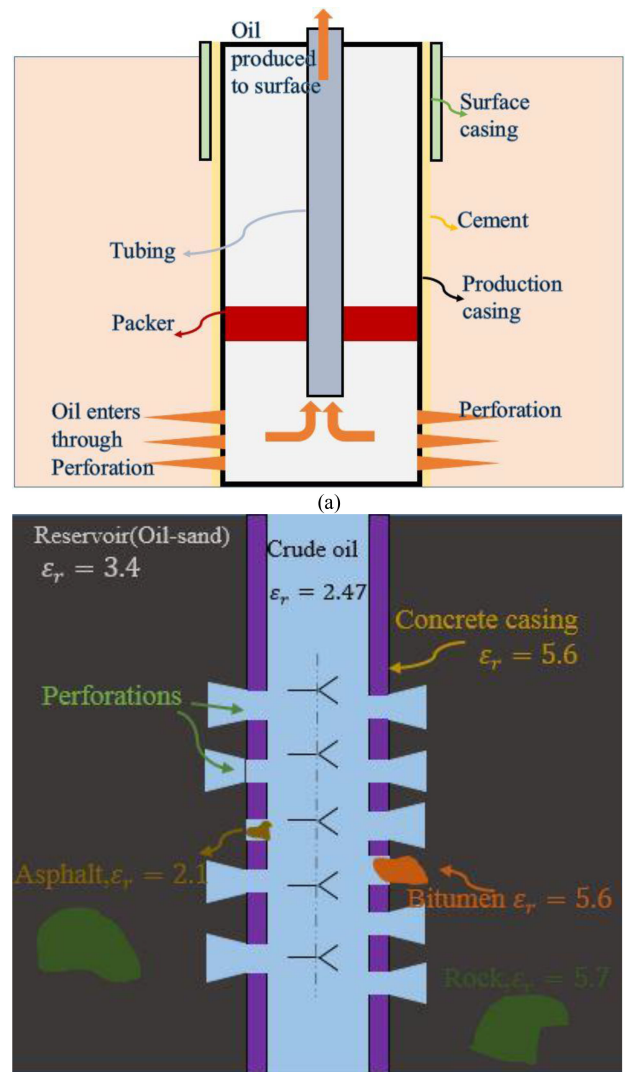

Fig. 1. (a) Oil well structure. (b) Production zone and radar imaging.

depends on reservoir characterization, but the diameter of hole is eventually decreased in the bottom of well hole leading to a conical shape. When a well is drilled it should be completed. Completion is a process that prepares oil well to produce oil and gas [31], [32].

A most important completion widely used is perforation completion. Perforation completion includes drilling the reservoir to desired depth, running the casing to the bottom of reservoir, cementing and perforating production casing to a design depth in reservoir to make a channel for flowing oil and gas from reservoir to well. Well casing as an important step in completion served for fortifying the well hole, preventing oil and gas leakage during pulling up to surface, and keeping other fluids and gases to seep into well. The oil well wall is covered by metal or concrete, or combination of them [31], [32].

Deepest region of the well is called production zone. In this region, the casing is perforated to allow hydrocarbons flow to well, but it provides considerable amount of protection for the borehole. Size of the production zone casing depends on

some considerations, but it is typically 5–28 cm. However, the diameter about 15 cm is more common. Depending on the depth and type of the oil well, perforation diameter varies 1–4 cm. The crude oil alongside with various byproducts such as water, gas, and other organic materials flows into the well. Conventional organic materials which can be found in the oil well are asphalt, rocks, sand, and bitumen that can block the perforations and reduce well production. Schematic of production zone is shown in Fig. 1(b) [31], [32].

Once the casing is completed, tubing is placed inside the well and a packer is installed between casing and tubing to fix it [see Fig. 1(a)]. Due to the high cost of drilling new wells, the oil and gas companies are interested to extend the oil well life by monitoring it [8].

In this article, a UWB SAR imaging system is proposed to monitor the oil well casing and perforation conditions drilled in oil well wall. These conditions can be open, fully or partially clogged which affect directly the oil well performance. In fact, the imaging is realized based on diversity of dielectric properties of existing material in the oil well. The dielectric properties of these materials are illustrated in Fig. 1(b). By regular scanning of oil well and evaluating the status of all perforations, if any impairment is observed, we can resolve this problem using solvents at an early stage to protect the well [32]. To image the oil well using SAR method, the sensor scans along its wall. By rotating the sensor around the well axis in azimuth plane and combining 2-D images, we can construct a 3-D image of the oil well. However, in this article, the sensor is moved only along well axis [see Fig. 1(b)] and does not rotate around it. So, we only perform 2-D imaging.

B. Scattering

In this application, we face various sources of clutter, which complicate imaging. In the following, the clutter sources are introduced.

First, due to imaging in a long cylinder, the medium mimics a cylindrical waveguide either concrete casing or metal casing. Therefore, when the Tx antenna radiates energy with a broadband spectrum, several waveguide modes excited simultaneously are received by the Rx antenna in addition to the scattered signals from the perforations.

Surface waves are the second source of clutter. The surface wave is a form of a traveling wave which follows the geodesic path of the surface of an object. If the wave meets an obstacle or a discontinuity such as gaps, slots, steps, and seams; the surface wave will be reflected [33].

According to GPR terminology, antenna coupling is also a source of clutter [34]. Due to size limitation, we cannot avoid placing the Tx and Rx antenna in close proximity of each other; so, a part of transmitted energy is induced on Rx antenna, directly. The coupling signal can hide the scattered from the target.

The fourth clutter source is the scattering from the interior surface of pipe. Due to the geometry restriction, we have to set the sensor in the middle of well, so in each scan, not only the target region in front of Tx/Rx antenna, but also the whole surrounding region is illuminated and the reflected waves by those unwanted regions are entered to the receiver as clutter. In addition, we face multi bounce reflections in the pipe geometry.

III. CLUTTER REDUCTION ALGORITHMS

Clutter is a group of signals, uncorrelated with the target signal, which fills the same spectrum as target signal. Therefore, it is difficult to distinguish them from each other, and some preprocessing steps are necessary to extract the target signal. To the best of our knowledge, clutter removal in tube and well imaging has not been investigated, yet. In this section, we describe some well-known clutter reduction techniques for radar imaging and then evaluate their performance.

In SAR imaging, we create a B-scan data matrix (Radargram) whose dimensions is $M \times N$ (M is the number of samples in each A-scan and N is the number of aperture positions/number of A-scans). The A-scan is a 1-D signal obtained in each scan position. B-scan is a 2-D signal resulted from putting A-scans alongside.

A. Mean Scan Subtraction

A simple method for clutter reduction is mean subtraction, which average of all A-scans or average of a part of A-scans is subtracted from B-scan data matrix. This method is used for removing stationary clutter [35].

B. L_1 Norm Subtraction

In this way, L_1 norm of all A-scans is calculated and the A-scan with the lowest L_1 norm is assumed as background signal. Then, it is subtracted from all other A-scans to remove the background signal, and similarly to the mean scan subtraction, this method is effective only for stationary clutters [28]. L_1 norm of a vector is defined as follows:

$$\|X\|_1 = \sum_i |x_i|. \tag{1}$$

C. SVD

Singular value decomposition is a matrix factorization method in linear algebra, which is used in various applications for noise reduction, compression, pattern detection, etc. In fact, SVD decomposes matrix into Eigen subspaces which are assumed to originate from different sources in each scenario [22]. The B-scan data matrix can be decomposed as follows:

$$X = U\Sigma V^H \tag{2}$$

where U and V are unitary matrices whose columns are the singular vectors of matrix X. H denotes the Hermitian operator and the matrix $\Sigma = \text{diag}(\sigma_1, \sigma_2, \ldots, \sigma_r)$ is a diagonal matrix, whose entries are the singular values of the matrix X sorted in descending order. In imaging applications, matrix X can be decomposed to r rank-1 subspaces as follows:

$$X = \sum_{i=1}^{r} \sigma_i u_i v_i^H = M_1 + M_2 + \cdots + M_r. \tag{3}$$

Each matrix M_i has the same dimension as the original matrix and typically map different sources such as signal, clutter, and noise. Therefore, by decomposing the data matrix and removing the subspaces related to noise and clutter, we can reconstruct the target signal. The clustering can be done manually or automatically, as described in [36].

D. 2-D Singular Spectrum Analysis

SSA is a model free technique proposed for analyzing time series. It is used for decomposing a time series to separable components such as a sum of trends, oscillations, and noise. This method has attracted much attention recently because of its capability in various areas such as climatology, meteorology, geophysics, engineering, and economics without any assumption on the data to provide meaningful results. For applying the algorithm to a set of time series, multivariate SSA was developed, and for applying on 2-D scalar fields, 2-D SSA version was developed. Recently, 2-D SSA has been used in image processing for reducing noise and extracting features and in radar area for removing clutter [37]–[45]; however, further research in these areas is required.

The implementation of all SSA versions is divided into four steps: embedding, decomposing, grouping, reconstructing. Various versions only differ in embedding and reconstructing steps. In the following, these four steps are explained briefly and finally a modified 2-D SSA for clutter reduction in oil well imaging is proposed.

1) Embedding: Assume 2-D data with a size $N_x \times N_y$ as follows [45]:

$$X = \begin{bmatrix} P_{1,1} & P_{1,2} & \cdots & P_{1,N_y} \\ P_{2,1} & P_{2,2} & \cdots & P_{2,N_y} \\ \vdots & \vdots & \ddots & \vdots \\ P_{N_x,1} & P_{N_x,2} & \cdots & P_{N_x,N_y} \end{bmatrix}. \tag{4}$$

Similar to 1-D SSA [29], a window needs to move over the data matrix to construct trajectory matrix. However, in 2-D SSA, the window is 2-D with a size $L_x \times L_y$. If we determine the window position by top-left corner (i, j), the window must be moved for each row i along all possible j column positions which is equal to $K_y = N_y - L_y + 1$. The path that window is moved, is row scanning from top-left to bottom-right of raw data matrix. Therefore, the number of positions is $K_x \times K_y$, where $K_x = N_x - L_x + 1$. Each window data W_{ij} can be represented as follows:

$$W_{i,j} = \begin{bmatrix} P_{i,j} & P_{i,j+1} & \cdots & P_{i,j+L_y-1} \\ P_{i+1,j} & P_{i+1,j+1} & \cdots & P_{i+1,j+L_y-1} \\ \vdots & \vdots & \ddots & \vdots \\ P_{i+L_x-1,j} & P_{i+L_x-1,j+1} & \cdots & P_{i+L_x-1,j+L_y-1} \end{bmatrix}. \tag{5}$$

To reconstruct trajectory matrix and avoid producing 4-D matrix each window matrix is reshaped to a column vector A_{ij}

as follows:

$$A_{i,j} = \begin{bmatrix} P_{i,j} \\ P_{i,j+1} \\ \vdots \\ P_{i,j+L_y-1} \\ P_{i+1,j} \\ \vdots \\ P_{i+L_x-1,j+L_y-1} \end{bmatrix}. \tag{6}$$

Finally, the trajectory matrix Y with size $L_x L_y \times K_x K_y$ is derived as follows:

$$Y = \begin{bmatrix} A_{1,1} & A_{1,2} & \cdots & A_{1,K_y} & A_{2,1} & \cdots & A_{K_x,K_y} \end{bmatrix} \tag{7}$$

The obtained trajectory matrix has Hankel block Hankel (HBH) form and is represented as follows:

$$Y = \begin{bmatrix} H_1 & H_2 & \cdots & H_{K_x} \\ H_2 & H_3 & \cdots & H_{K_x+1} \\ \vdots & \vdots & \ddots & \vdots \\ H_{L_x} & & \cdots & H_{N_x} \end{bmatrix} \tag{8}$$

where

$$H_r = \begin{bmatrix} P_{r,1} & P_{r,2} & \cdots & P_{r,K_y} \\ P_{r,2} & P_{r,3} & \cdots & P_{r,K_y+1} \\ \vdots & \vdots & \ddots & \vdots \\ P_{r,L_y} & P_{r,L_y+1} & \cdots & P_{r,N_y} \end{bmatrix}. \tag{9}$$

Note that each H_r block has Hankel format, which must be considered in the final step to reconstruct the desired data matrix, properly.

2) SVD: The second step of decomposition is performing SVD on trajectory matrix as described in Section III-C. Matrix E_i corresponds to each set of u_i, v_i from U, V matrix calculated as follows:

$$E_i = u_i v_i^T \tag{10}$$

and the data matrix X is obtained as follows:

$$X = \sum_i \sigma_i E_i. \tag{11}$$

3) Grouping: In this step, the elementary matrices E_i are jointed into T groups, and in each group they are added together to reconstruct a new set of matrices $D_j, j = 1, 2, 3, \dots, T$. In this article, we used *k*-means and hierarchical clustering [36] to automatically group the elementary matrices.

4) Reconstruction: This step is also called diagonal averaging. The obtained matrices D from grouping stage are not necessarily in HBH format, so similar to 1-D case, we have to perform Hankelization with some modifications for 2-D case as follows. To this end, a two-step Hankelization should be

carried out. First, Hankelization is performed between blocks [the blocks in (8)] and then Hankelization is applied within each block (9). Finally, as it is clear from trajectory matrix, each element from original raw data is repeated several times in trajectory matrix. Therefore, after Hankelization, by averaging among the values corresponding to the same elements in the reconstructed trajectory matrix, the reconstructed data from each group D_j is obtained as follows:

$$X^j_{\text{recon}} = \begin{bmatrix} R^j_{1,1} & R^j_{1,2} & \cdots & R^j_{1,N_y} \\ R^j_{2,1} & R^j_{2,2} & \cdots & R^j_{2,N_y} \\ \vdots & \vdots & \ddots & \vdots \\ R^j_{N_x,1} & R^j_{N_x,2} & \cdots & R^j_{N_x,N_y} \end{bmatrix}. \quad (12)$$

Note that the original data can be obtained by

$$X = X^1_{\text{recon}} + X^2_{\text{recon}} + \cdots + X^T_{\text{recon}}. \quad (13)$$

E. Modified 2-D SSA

As described earlier, the first step of any type of SSA corresponding to construct the trajectory matrix is realized by moving a window on the original data. Therefore, because of embedding step, the target effect is distributed on the trajectory matrix. Since each cluster is representative of different sources in the imaging scene including clutter, multipath, nearly object, etc., or in other words, different eigen values; the reconstructed image from each cluster are illustrating these different sources of scene. To alleviate this effect, we add an additional step to clutter removal method using 2-D SSA as follows: after applying 2-D SSA on the raw data and constructing the image of different clusters using GBP, the images related to target, are multiplied by each other to remove artifacts. Since the real image is constant in all selected clusters and artifacts usually appears with different placements in different clusters, this multiplication removes artifacts and keeps the real image. Note that the target we want to reconstruct its image has a simple geometry; so the image multiplication does not corrupt the shape of target. As stated in [46], this method is applicable only for simple target geometries not the complex ones. We call the whole algorithm—2-D SSA and image multiplication—as "modified 2-D SSA."

In the literature, image multiplication was introduced for different goals such as clutter removal, multipath suppression, and artifact removal [46]–[48]. In [46], to eliminate artifacts, which are created during image reconstruction, two images from different view are multiplied to each other. One image is reconstructed from front view of target and the other is reconstructed from rear view. In [47], to remove multipath in through wall imaging applications, two sub aperture images multiplied to the original full aperture image. In [48], a Ground Base-SAR is used for foreign object detection, and the clutter is removed by multiplying reconstructed original image and a filtered image with some processing.

The next section will investigate the performance of these clutter removal methods for oil well imaging problem.
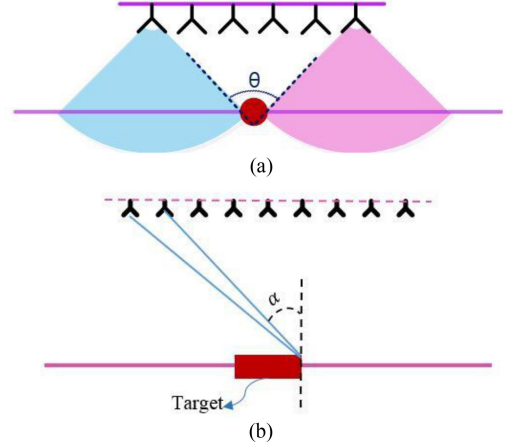

Fig. 2. (a) Schematic of strip map SAR system. (b) Sampling criteria.

IV. EVALUATION OF CLUTTER REMOVAL ALGORITHMS

In this section, first, SAR system parameters are introduced briefly. Next, full-wave simulation of an oil well is performed using CST MWS software to investigate the performance of clutter reduction algorithms.

A. SAR System

The schematic of SAR system is shown in Fig. 2(a). In SAR, the transceiver is moved along the aperture and receives the reflected signal from target scene. Two important design parameters that should be considered are sampling distance and image resolution.

1) Spatial Sampling: Spatial Nyquist sampling criteria ensures alias-free image. Based on this theory, the phase difference between two successive aperture positions must be less than π. In quasi monostatic scenario like Fig. 2(b), the maximum phase difference occurs between opposite edge of target scene and aperture. In this way, the maximum sampling distance can be calculated as follows:

$$dx = \frac{\lambda}{4\sin\alpha} \quad (14)$$

where λ is the maximum frequency, and α is depicted in Fig. 2(b). In the worst-case scenario ($\alpha = 90°$), to ensure an alias free image, the maximum distance between two aperture positions must be less than $\lambda/4$ [49].

2) Image Resolution: In SAR imaging, two important factors are cross-range and down range resolution. The cross-range resolution is defined as resolution alongside the aperture and is calculated as follows:

$$\delta_{Xr} = \frac{\lambda_c R}{2L} \quad (15)$$

where λ_c is the wavelength of center frequency, R is the perpendicular distance between aperture line and scene, and L is the effective aperture length. The down range resolution is the resolution of radar in direction perpendicular to aperture and
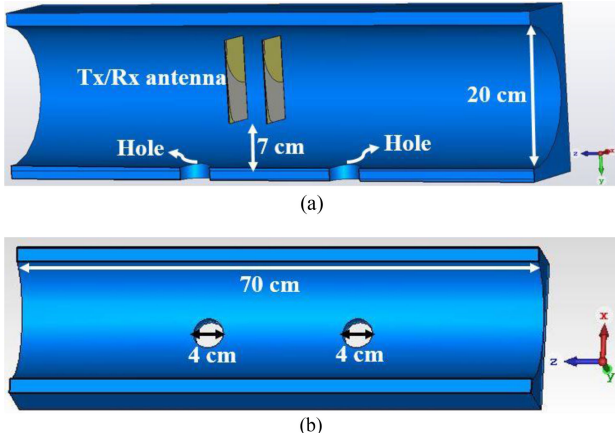
Fig. 3. Schematic of oil well monitoring system. (a) Cross view. (b) Top view.

depends on signal bandwidth as follows:

$$\delta_{dr} = \frac{C}{2Bw} \qquad (16)$$

where C is the speed of light in medium and Bw is 3 dB frequency bandwidth [49].

3) Image Reconstruction: The SAR image reconstruction algorithms are divided in two categories of frequency domain and time domain. Among frequency domain approaches, the wavenumber-domain approaches e.g., holography [50] has high accuracy [51]. However, for wavenumber-domain algorithms, it is necessary that the data to be resampled in k_z − space. To avoid this resampling, and improving the accuracy, Amineh *et al.* [52], [53] proposed putting 2-D slices of holographic image together and reconstruct a 3-D image, which make the procedure complicated. To avoid this complexity, here, we use GBP (without any far-field approximation in phase) which is a time domain approach. The disadvantage of GBP is its time consumption. However, since the scene in pipe monitoring is not too large, GBP still provides real-time image. In order to implement GBP, first, the scene is gridded based on desired resolution. Then, the intensity of each pixel is calculated by coherent summation of related time sample of all aperture positions. In each pixel, the relative time samples are obtained by calculating round trip time from the pixel to every aperture position. From mathematical view, the image of scene is reconstructed by the integral

$$h\left(x_0, r_0\right) = \int_{\frac{-L}{2}}^{\frac{+L}{2}} g(x, R) dx$$

where $h(x_0, r_0)$ is the backprojected signal as a function of pixel position (x_0, r_0), L is the aperture length, g is the radar echo as a function of aperture position x and distance between pixel and aperture position R.

B. Full-Wave Simulation and Algorithms Performance

The simulated oil well structure is shown in Fig. 3. The pipe casing is made of concrete; the diameter of well is 20 cm and its thickness is 2.5 cm. As illustrated in Fig. 3, two holes with diameter of 4 cm have been perforated in the well wall with 25 and 45 cm distance, respectively, from right edge of pipe.
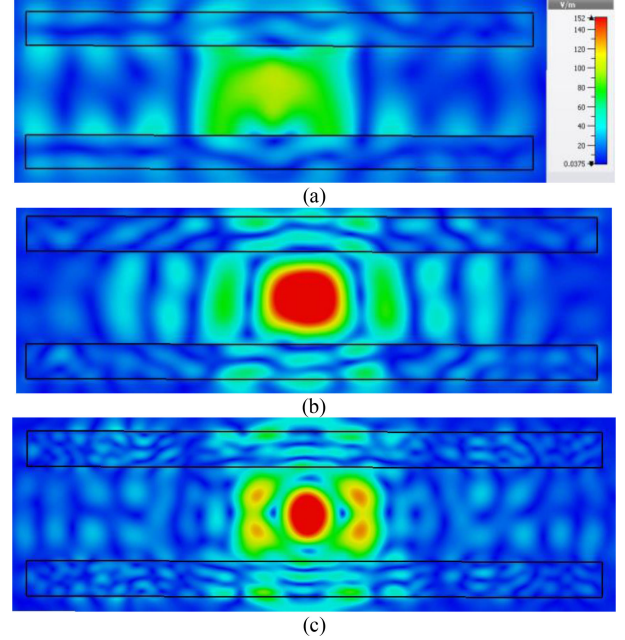

Fig. 4. E-Field distribution in the well in a plane 7 cm below the antenna at (a) 2, (b) 3, and (c) 5 GHz.

The transmitter/receiver antenna is a Vivaldi antenna with the impedance bandwidth from 2.2 to 12 GHz separated 5 cm from each other. Their distance from the interior surface of well wall is 7 cm. Since the simulation structure is big (70 cm well length) we reduce the simulation bandwidth to run our simulation in lower time. Therefore, in each aperture position, a broadband pulse with the bandwidth of 2.2–6.7 GHz is emitted by Tx antenna, and Rx antenna receives: reflections from target, coupling from transmitter antenna and other unwanted clutter signals. The radar system is quasi monostatic, and Tx/Rx antennas are shifted along the well wall every 1 cm which satisfy Nyquist spatial sampling criteria.

E-Field distribution in the well in XZ plane [see Fig. 3(b)] 7 cm below the antenna in Y direction is illustrated in Fig. 4 for 2, 3, and 5 GHz. As can be seen, in a limited region, the field is approximately uniform which mimics plane wave. It is an important criterion in imaging; all targets in this region receive approximately the same in phase signal. Therefore, the size of this region is the effective footprint of antenna.

Raw data and reconstructed image by GBP—without any clutter removal—are illustrated in Fig. 5. Fig. 5(a) is image of B-scan matrix. In all images, the dashed line squares show the position of real perforations. As can be seen, the strongest received signal is the coupling from Tx antenna.

Now, we apply the proposed clutter removal techniques on raw data and then apply GBP to reconstruct the image. The reconstructed image resulted from mean scan subtraction and L_1 norm techniques are shown in Fig. 6(a) and (b), respectively. As can be seen, in this scenario, the mean subtraction method shows better result.

Here, we perform SVD on raw data and decompose it to some singular values and singular vectors correspond to different sources in simulated scenario, i.e. clutter, target, and noise.
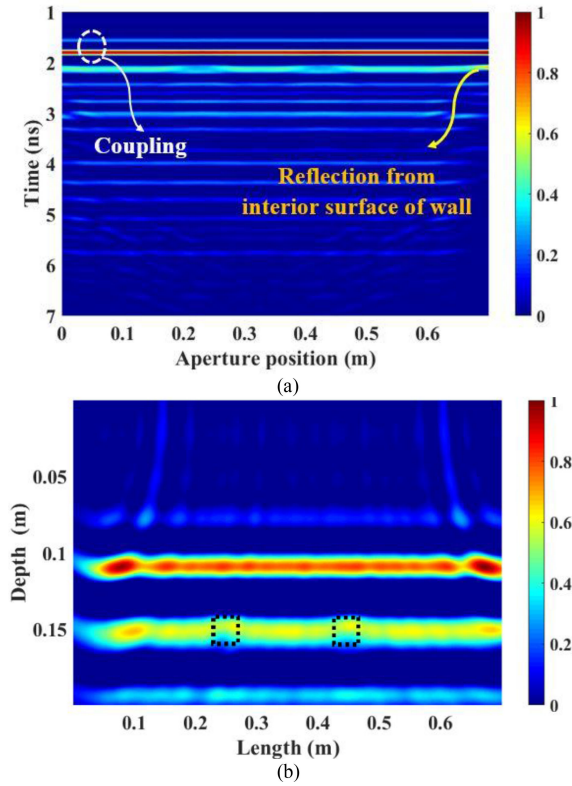
Fig. 5.   (a) Raw data and (b) reconstructed image without any clutter removal.

We define $\sigma_i/\sigma_1 \leq 0.001$ as a noise subspace. Therefore, we removed related singular values to this subspace. We found that the first two singular values correspond to static clutter of antenna coupling and reflection from interior surface of the wall; so, they were removed. Finally, the reconstructed image by remained singular values is shown in Fig. 6(c). As shown, mean subtraction and SVD show almost similar performance while SVD result is a little better.

One of the principal parameters of SSA is window length selection that affects the orthogonality of subseries of primary series and closeness of singular values. However, there is no general rule for determination of window length in imaging applications, though some general principles for some applications such as trend extraction, smoothing, and periodicity extraction reported in the literature [40], [54]. Therefore, we evaluate the effect of window length in perforation imaging. It is seen that by increasing the window length, some replicas of perforation appear in the reconstructed image. On the contrary, very small lengths leads to missing of information. Finally, we choose $L_x = L_y = 15$ as the windows length. For the sake of brevity, we only present the results of investigation; not their images. Similar to window length, there is no theoretical rule to find optimal number of clusters. After testing various number of clusters, we found that to attain good results in terms of minimum artifact, the number of clusters should be more than half of their maximum number. In this simulation, it is assumed 16. In Fig. 7, the reconstructed images after applying basic 2-D SSA and modified 2-D SSA are illustrated. Among different clusters, the image of two clusters of 14 and 15 are related to coupling and
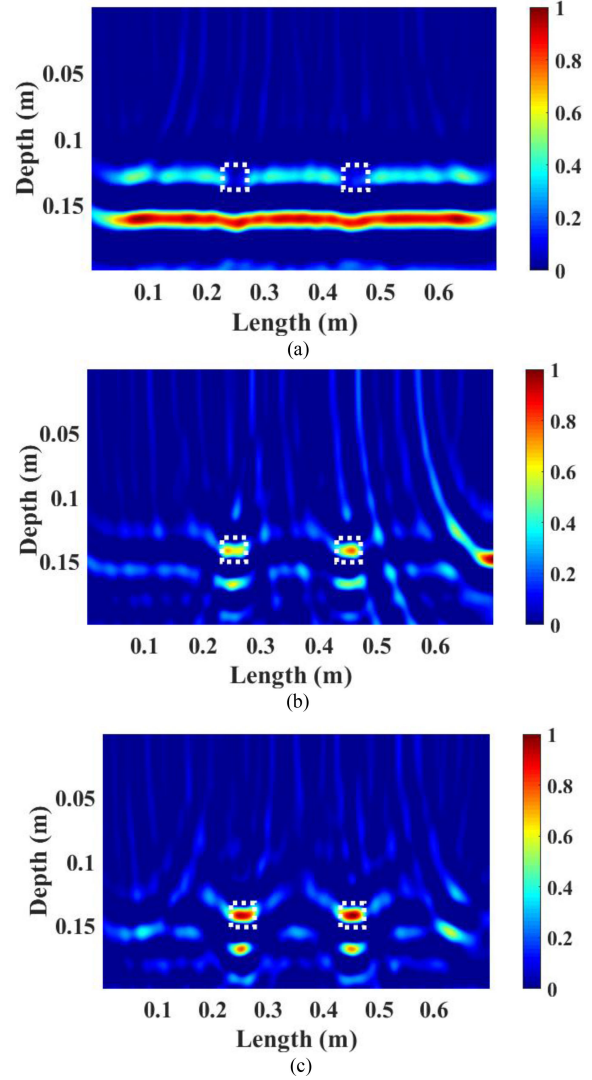

Fig. 6.   Reconstructed image after clutter reduction using (a) L1norm, (b) mean scan subtraction, and (c) SVD.

TABLE I
SCR AND CONTRAST OF DIFFERENT CLUTTER REMOVAL METHODS

	L$_1$norm	Mean subtraction	SVD	Modified 2D-SSA
SCR	-7	10.28	13.03	22.99
Contrast	-19.7	-2.3	4.87	15.38

reflection from interior surface of wall, clusters 11–13 include target and some artifacts, and the remained clusters present images including too much artifacts which are not shown for the sake of brevity. As can be seen, in clusters 11–13, some artifacts due to applying 2-D SSA are produced. These artifacts are removed by multiplication of image of clusters 11–13 (Modified 2-D SSA). The results of modified 2-D SSA is shown in Fig. 7(f).

To compare these algorithms in this application quantitatively, SCR and contrast of each image are listed in Table I. The SCR is evaluated by (17) [19], and the contrast is defined as the ratio between value of two pixels with highest intensity in the target
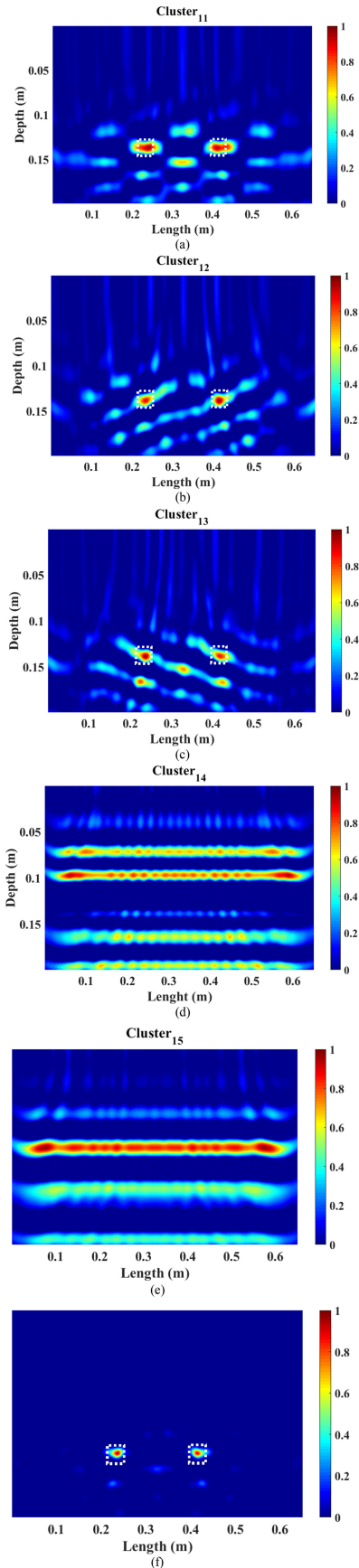
Fig. 7. Reconstructed image using 2-D SSA. (a) Cluster11. (b) Cluster12. (c) Cluster 13. (d) Cluster 14. (e) Cluster 15. (f) Modified 2-D SSA.

region and background.

$$\text{SCR} = \frac{\frac{1}{N_t} \sum_{(x,z) \in A_t} |\rho(x,z)|^2}{\frac{1}{N_c} \sum_{(x,z) \in A_c} |\rho(x,z)|^2} \qquad (17)$$

where A_t and A_c are target and clutter regions, respectively, N_t and N_c are number of pixels in target and clutter regions, and ρ is the intensity of pixel. As can be seen in Table I, modified 2-D SSA outperforms the other clutter removal methods.

The observed behavior is explainable by mechanism of each algorithm. Both L1-norm and mean subtraction are only suitable for stationary clutter removal. However, mean subtraction is better than L1-norm subtraction. The reason is that in L1-Norm subtraction, we subtract the A-scan with minimum L1-norm from all data matrix. In this case, if one aperture position get very weak signal, e.g., physical phenomena or even noise/random error, that position would be the determinative and if it does not see the effect of a stationary clutter, that stationary clutter would not be removed by this method. As can be seen in Fig. 6(a), the effect of wall has not be removed by this method. However, in mean scan subtraction, the average of all signal in all aperture positions is determinative and if the effect of a stationary clutter isn't sensed in some points, it could still be removed because of its effect in other points. As can be seen in Fig. 6(b), this method removes the effect of wall. SVD and SSA as blind source separation algorithms, can differentiate among different targets in the scene and are effective on both stationary and nonstationary. Compared to SSA, SVD needs less computational times but is less powerful.

V. PROPOSED ALGORITHM FOR IMAGING

In the previous section, we investigated different clutter removal methods. However, in addition to clutter removal, some preprocessing steps have to be done on raw data. The proposed comprehensive algorithm is shown in Fig. 8. The first step is coupling removal. Actually, we have two general types of clutter in this SAR imaging case: stationary & nonstationary. Stationary clutters are those constant clutters in all scan point of SAR, e.g., coupling and holder scattering. Nonstationary clutters are those that vary over different SAR scan points, e.g., effect of well edge and higher-order scattering in the waveguide. Although SVD-based algorithms are able to remove both stationary and nonstationary clutters, removing the coupling effect which usually has the highest energy contribution and highest singular value, makes the dynamic range of remaining part of signal smaller and therefore, handling of the remaining singular values becomes easier. There are different methods for coupling removal. In the literature, typical method is that the received signal is measured without target in desired medium (ambient measurement); however, it is hardly possible in real scenario of oil well monitoring. Instead, we choose L_1 norm for coupling removal.

In the second step, we should determine optimum scan length. In oil well monitoring which mimics a strip map SAR, depending on the antenna footprint, we have a limited effective length. It means that because of the limited footprint of antenna on scene, Rx antenna only receives reflection of each perforations in a
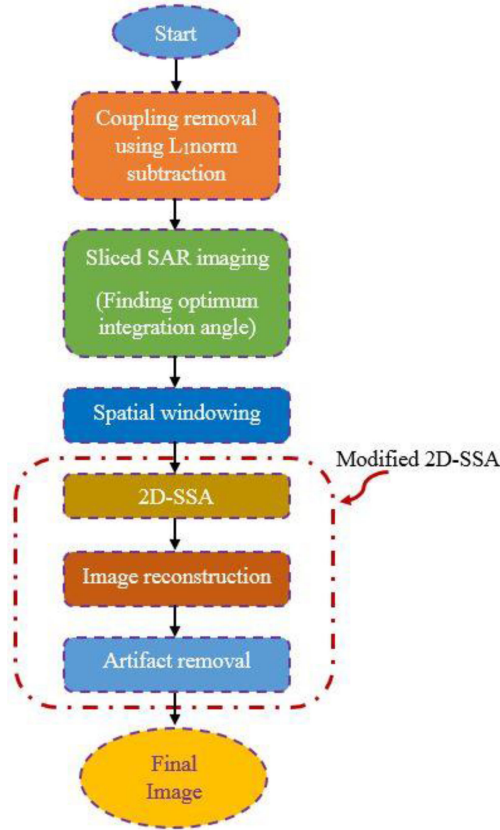
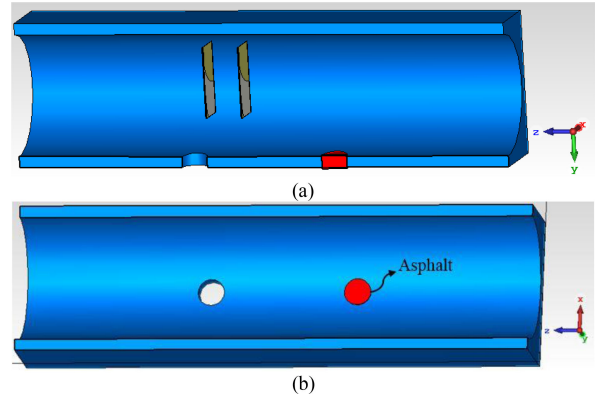Fig. 8. Flowchart of the proposed algorithm.

Fig. 9. Schematic of simulated structure. (a) Cross view. (b) Top view.

Fig. 10. Reconstructed Image of oil well structure with open and clogged perforations.

limited scan length and the received signals from outside of this effective scan length play role of clutter for that part of image [see Fig. 2(a)]. Therefore, we should reconstruct image of each perforation separately with limited scan length, not using all A-scans. For far-field SAR imaging, there are analytic formulas for integration angle [θ in Fig. 2(a)]; however, there is not any formula for near-field SAR imaging. On one hand, higher integration angles increase the clutter level and we have to reduce integration angle. On the other hand, the cross-range resolution depends on scan length or integration angle and we are not allowed to overcut the integration angle. Therefore, to find the optimum scan length, we propose sliced SAR imaging whereas we slice the scan length to some equal parts and construct the image of each slice, separately.

After calculating the optimum scan length, we perform spatial windowing. To this end, we window each A-scan signal and select a part of signal scattered from the desired perforation neither scattering from closer nor farther objects. The next step in signal processing chain is applying a clutter reduction method. According to results of the previous section, modified 2-D SSA has the best performance. Therefore, we use it as clutter reduction method whereas, first 2-D SSA is applied. Then, the image is reconstructed. Since 2-D SSA creates some artifacts, the last step of modified 2-D SSA (artifact removal, i.e., multiplication of image of different clusters) is applied.

In order to verify the effectiveness and repeatability of proposed method in pipeline monitoring, another full wave

simulation using CST Microwave Studio is done. The simulated oil well structure is shown in Fig. 9. All simulation parameters are like previous simulation, but the only difference is concerned with one of the perforations. In this scenario, the second hole is clogged by an asphalt cylinder which its electrical characterization is assumed as $\varepsilon_r = 2.1, \sigma = 0.05$. The asphalt cylinder fills the second hole, completely.

Like previous simulation, the window length and the number of clusters in 2-D SSA are assumed as $L_x = L_y = 15$, and $n_c = 16$, respectively. Final image is reconstructed by multiplying images produced by clusters 9–11 which include target information. The reconstructed image using proposed algorithm is illustrated in Fig. 10. For the sake of brevity, only the final image is shown and not the image of all clusters. As it can be seen, the intensity of the second hole is weaker than the first hole which means the second hole is clogged by a foreign object. Since asphalt and concrete have different permittivities, it makes sense that footprint of the second hole in the image has a weaker intensity compared to the first hole because of the lower permittivity difference between concrete and asphalt.

VI. MEASUREMENT

In this section, to verify the proposed algorithm, a practical setup is developed. Due to executive difficulties, we do not fill the well with oil. However, since the oil is almost lossless and nondispersive [55], considering it will not affect the results except a possible improvement due to its permittivity which
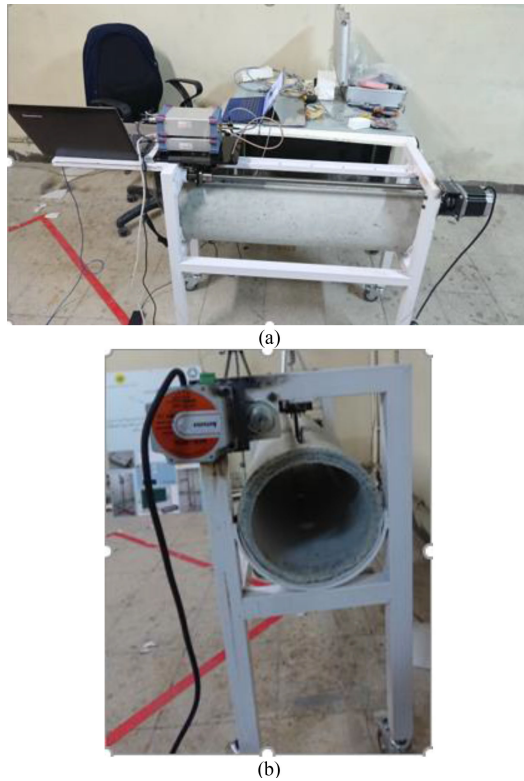
(a)

(b)

Fig. 11.   Oil well positioner. (a) Side view. (b) Cross view. (c) UI.

makes near-field range shorter. Different parts of measurement setup are described as follows.

A. Oil Well Positioner

The oil well positioner is shown in Fig. 11. It includes concrete pipe, stepper motor, ball screw, boring, a standing structure, and Arduino board as a processor. We first describe the mechanic and then electronic section.

First, rotational movement of stepper motor is transformed on ball screw using two pulleys and timing belt. Ball screw translates rotational movement of motor to transitional movement. Screw is fixed using two borings at the beginning and end to rotate around itself. Ball screw is connected to a linear motion guide that carries a Plexiglas shaft. On the top of pipe, a groove is cut; so, the shaft can enter the pipe and move freely along it. The Tx/Rx antennas are attached to the end of the shaft. The motor model is chosen such that to transform the shaft with precision of the order of sub millimeter. On the top of ball screw, a planar platform is fixed to carry UWB sensor during scan.

In the electrical section, a user interface is developed to be a bridge among user, sensor, and motor. The user can set measurement parameter and control positioner by a user interface (UI). The UI sends current position of the antenna to the Arduino board based on positions entered by user including start position, stop position, and step. The Arduino board translates these commands for motor driver in a form of pulsewidth modulation pulse. When the UI sends the commands to Arduino and motor relaxes in the desired position, it sends the "save" command to sensor.
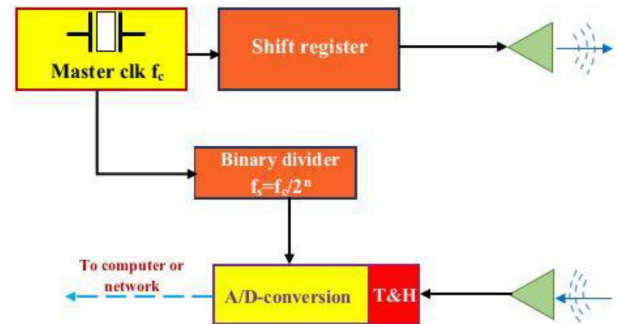

Fig. 12.   Block diagram of M-sequence sensor.

TABLE II
PLACEMENTS AND RADIUSES OF PERFORATIONS FABRICATED IN OIL WELL PIPE MODEL

L1(cm)	R1(cm)	L2(cm)	R2(cm)
20	2	52	1.5

B. UWB Sensor

A Maximum length sequence (M-sequence) sensor (m: explore form Ilmsens company [56]) is used. It has simple structure, high measurement speed, high stability, and low crest factor signal. In this technique, energy of pulse is distributed over the time, and therefore, maximum amplitude of signal is low. The low amplitude simplifies circuit and improves RF behavior. The block diagram of sensor is shown in Fig. 12. A binary divider controls subsampling. In this method, thanks to steep pulse edges of binary divider, drift and jitter are suppressed significantly, and it avoids nonlinear sample spacing. The shift register with its feedback produces a M-sequence signal with high instantaneous bandwidth. This signal is periodically applied to the target and data gathering is implemented by undersampling method. A brief description of sensor will be described as follows [57].

Maximum length binary sequence is one of the pseudo random binary sequence signals used as stimulus in several applications due to its short triangular autocorrelation function that provides acceptable resolution and low side lobe level. The M-sequence signal, its spectrum and autocorrelation are shown in Fig. 13.

f_c is the clock frequency of shift register with length of n. Regarding to length of shift register, signal is constructed from $N = 2^n - 1$ chip in each period of M-sequence. Spectrum envelope of M-sequence signal is $\sin c^2$ function, and 80% of signal energy is distributed between $\mathrm{DC} - \frac{f_c}{2}$.

VII. RESULTS

In this section, some measurement scenarios are implemented and the results are illustrated. The concrete pipe length is 98 cm and the inner and outer diameter are about 22 and 25 cm, respectively. The perforations position (L1 cm and L2 cm from right edge of pipe) and radius (R1, R2) are illustrated in Table II.

During the scan, the distance between aperture positions is set to 5 mm, which satisfies (14). The clock frequency of M-sequence sensor, fc, is 18 GHz; therefore, the effective bandwidth is 9 GHz. The length of shift register is 9 bit; thus, in each
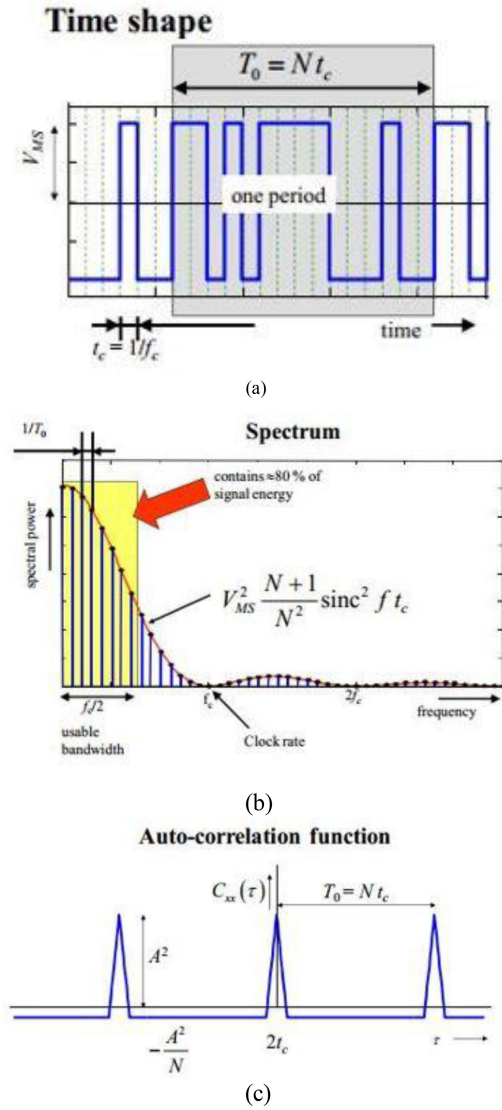
Fig. 13. M-sequence signal. (a) Its time shape signal, (b) spectrum, and (c) auto correlation function, reprinted from [57].

period of signal, we have 511 chip. Autocorrelation is done in the sensor hardware, so the shape of received signal is like Fig. 13(c). Note, to reconstruct the image properly, we have to adjust zero time in GBP algorithm for picking up the samples from each aperture position signal, based on this zero time. The first time that the amplitude of received signal reaches more than noise level can be supposed as zero time.

For 2-D SSA, the window size is $L_x = L_y = 15$ and the number of clusters is assumed 16. Our goal is to reconstruct image of well wall with at least 1 cm cross-range resolution. Therefore, based on (15) as a rough estimation of resolution and explanation given in Section V about finding optimum scan length, after some tuning, we selected 30 cm as the optimum scan length.

The raw data and some measured signals in different aperture position are shown in Fig. 14. As can be seen in Fig. 14(a) and (b), there is a strong coupling which is almost constant
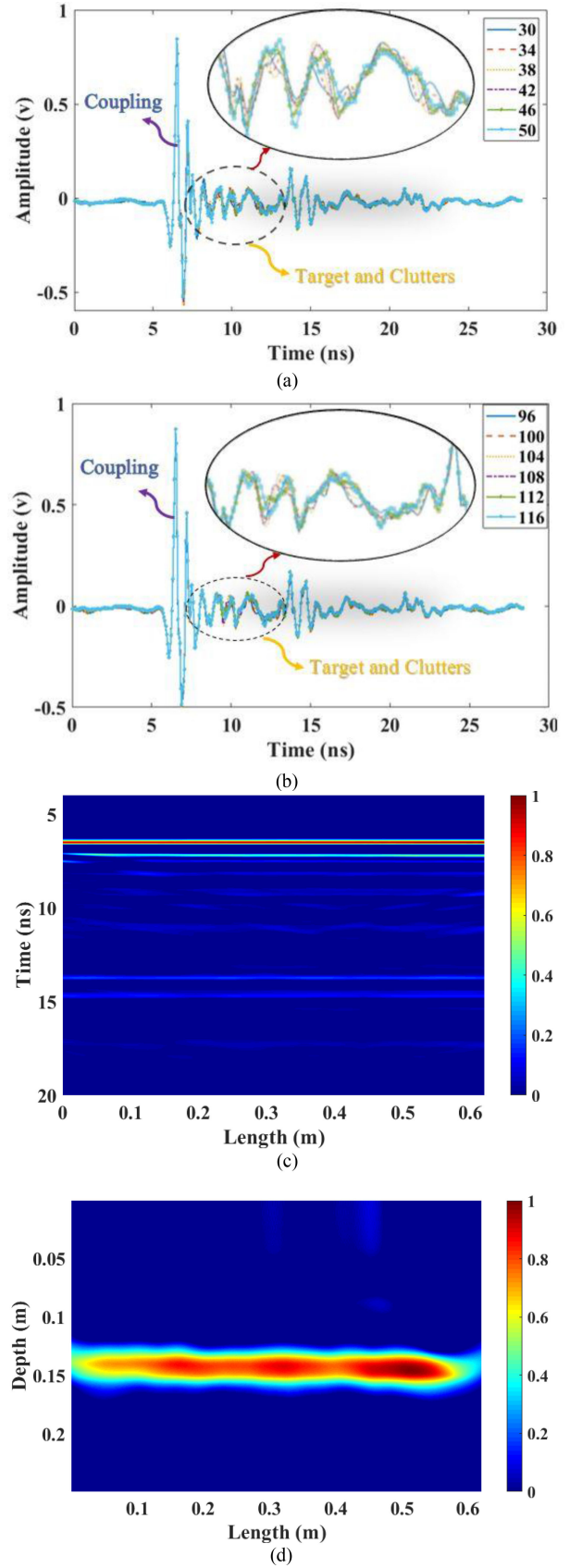
Fig. 14. (a) Some measured signals in first slice. (b) Some measured signals in second slice. (c) Measured raw data. (d) Reconstructed image without clutter removal.
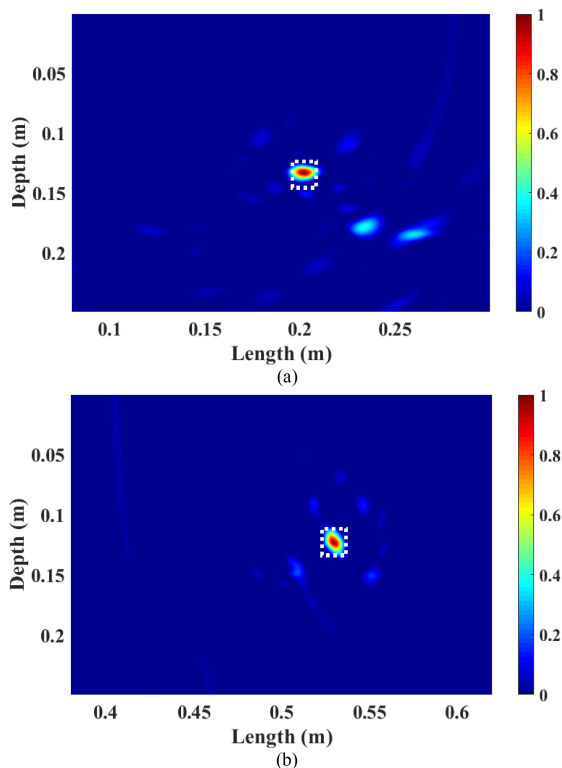
Fig. 15. Reconstructed image using proposed algorithm (a) perforation P1, and (b) perforation P2.

in different scan points. After this strong coupling, signals including the information of target, clutters and noise are visible. As can be seen, this part varies for different position and after processing and clutter reduction, provides image of perforations. The reconstructed images after proposed algorithm are shown in Fig. 15. The image of two perforations related to each slice are shown in Fig. 15(a) and (b).

VIII. CONCLUSION

Oil well monitoring faces various clutter sources due to geometrical restrictions which complicates imaging. For the first time, we compared some clutter removal algorithms in oil well imaging using UWB near-field SAR method, and proposed modified 2-D SSA for clutter removal. The performances of algorithms were investigated using full wave simulation data in where perforations are all open. Finally, a comprehensive algorithm for oil well imaging was proposed and its performance was verified by a different simulation case where perforations were open and clogged by asphalt material. Also, the performance was evaluated by experimental results.

REFERENCES

[1] C. Ékes, "Application of pipe penetrating radar for asbestos cement pipe condition assessment," in *Pipelines 2018: Condition Assessment, Construction, and Rehabilitation*. Reston, VA, USA: Amer. Soc. Civil Eng., 2018, pp. 183–190.

[2] C. Ekes and B. Neducza, "Pipe condition assessments using pipe penetrating radar," in *Proc. 14th Int. Conf. Ground Penetrating Radar*, 2012, pp. 840–843.

[3] Z. Liu and Y. Kleiner, "State of the art review of inspection technologies for condition assessment of water pipes," *Measurement*, vol. 46, no. 1, pp. 1–15, 2013.

[4] C. Ékes, B. Neducza, and P. Takacs, "Pipe penetrating radar inspection of large diameter underground pipes," in *Proc. 15th Int. Conf. Ground Penetrating Radar*, 2014, pp. 368–371.

[5] R. N. Deo, R. M. Azoor, and J. K. Kodikara, "Proof of concept using numerical simulations for pipe corrosion inferences using ground penetrating radar," in *Proc. 9th Int. Workshop Adv. Ground Penetrating Radar*, 2017, pp. 1–5.

[6] V. Donazzolo and R. Yelf, "Determination of wall thickness and condition of asbestos cement pipes in sewer rising mains using surface penetrating radar," in *Proc. 13th Int. Conf. Ground Penetrating Radar*, 2010, pp. 1–5.

[7] C. Ékes, B. Neducza, and G. R. Henrich, "GPR goes underground: Pipe penetrating radar," in *Proc. North Amer. Soc. Trenchless Technol. (NASTT) No-Dig Show 2011*, Washington, DC, USA, Mar. 27–31, 2011, pp. 1–10.

[8] D. Oloumi, M. I. Pettersson, P. Mousavi, and K. Rambabu, "Imaging of oil-well perforations using UWB synthetic aperture radar," *IEEE Trans. Geosci. Remote Sens.*, vol. 53, no. 8, pp. 4510–4519, Aug. 2015.

[9] C. Guo and R. C. Liu, "A borehole imaging method using electromagnetic short pulse in oil-based mud," *IEEE Geosci. Remote Sens. Lett.*, vol. 7, no. 4, pp. 856–860, Oct. 2010.

[10] D. Oloumi and K. Rambabu, "Metal-cased oil well inspection using near-field UWB radar imaging," *IEEE Trans. Geosci. Remote Sens.*, vol. 56, no. 10, pp. 5884–5892, Oct. 2018.

[11] Y. H. Chen and M. L. Oristaglio, "A modeling study of borehole radar for oil-field applications," *Geophysics*, vol. 67, no. 5, pp. 1486–1494, 2002.

[12] H. Yang, T. Li, Z. He, and Q. H. Liu, "Impulse borehole radar imaging based on compressive sensing," *IEEE Geosci. Remote Sens. Lett.*, vol. 12, no. 4, pp. 766–770, Apr. 2014.

[13] T. J. Li, H. N. Yang, Q. Zhao, and Z. O. Zhou, "Development of a single-borehole radar for well logging," *Telkomnika*, vol. 10, pp. 1–985, 2012.

[14] M. Miorali, E. Slob, and R. Arts, "A feasibility study of borehole radar as a permanent downhole sensor," *Geophys. Prospecting*, vol. 59, no. 1, pp. 120–131, 2011.

[15] F. Fioranelli, "Through-the-wall detection using ultra wide band frequency modulated interrupted continuous wave signals," Ph.D. dissertation, Durham Univ., Durham, U.K., 2013.

[16] B. Vuksanovic, "GPR image decluttering using matrix pencil based trace filtering method," *Int. J. Electron. Elect. Eng.*, vol. 4, no. 4, pp. 359–364, 2016.

[17] K. C. Ho, L. Carin, P. D. Gader, and J. N. Wilson, "An investigation of using the spectral characteristics from ground penetrating radar for landmine/clutter discrimination," *IEEE Trans. Geosci. Remote Sens.*, vol. 46, no. 4, pp. 1177–1191, Apr. 2008.

[18] P. Sharma, S. P. Gaba, and D. Singh, "Study of background subtraction for ground penetrating radar," in *Proc. Nat. Conf. Recent Adv. Electron. Comput. Eng.*, 2016, pp. 101–105.

[19] M. Garcia-Fernandez *et al.*, " SVD-based clutter removal technique for GPR," in *Proc. IEEE Antennas Propag. Soc. Int. Symp. Proc.*, 2017, pp. 2369–2370.

[20] N. Smitha and V. Singh, "Clutter reduction using background subtraction of ground penetrating radar for landmine detection," in *Proc. Asia Pac. Conf. Postgrad. Res. Microelectron. Electron.*, 2016, pp. 11–16.

[21] R. Solimene, A. Cuccaro, A. Dell'Aversano, I. Catapano, and F. Soldovieri, "Ground clutter removal in GPR surveys," *IEEE J. Sel. Topics Appl. Earth Observ. Remote Sens.*, vol. 7, no. 3, pp. 792–798, 2014.

[22] P. K. Verma, A. N. Gaikwad, D. Singh, and M. J. Nigam, "Analysis of clutter reduction techniques for through wall imaging in UWB range," *Prog. Electromagn. Res.*, vol. 17, pp. 29–48, 2009.

[23] V. Kabourek, P. Černý, and M. Mazánek, "Clutter reduction based on principal component analysis technique for hidden objects detection," *Radioengineering*, vol. 21, no. 1, pp. 464–470, 2012.

[24] D. Potin, E. Duflos, and P. Vanheeghe, "Landmines ground-penetrating radar signal enhancement by digital filtering," *IEEE Trans. Geosci. Remote Sens.*, vol. 44, no. 9, pp. 2393–2406, Sep. 2006.

[25] A. van der Merwe and I. J. Gupta, "A novel signal processing technique for clutter reduction in GPR measurements of small, shallow land mines," *IEEE Trans. Geosci. Remote Sens.*, vol. 38, no. 6, pp. 2627–2637, Nov. 2000.

[26] A. Hyvarinen, J. Karhunen, and E. Oja, *Independent Component Analysis*. Hoboken, NJ, USA: Wiley, 2001.

[27] B. Vuksanovic, "GPR image decomposition using two-dimensional singular spectrum analysis," in *Proc. 9th Int. Symp. Image Signal Process. Anal.*, 2015, pp. 288–293.

[28] F. Bonitz, M. Eidner, J. Sachs, R. Herrmann, and H. Solas, "UWB-radar sewer tube crawler," in *Proc. 12th Int. Conf. Ground Penetrating Radar*, 2008.

[29] J. Zabalza *et al.*, "Novel two-dimensional singular spectrum analysis for effective feature extraction and data classification in hyperspectral imaging," *IEEE Trans. Geosci. Remote Sens.*, vol. 53, no. 8, pp. 4418–4433, Aug. 2015.

[30] L. J. Rodríguez-Aragón, A. Zhigljavsky, L. J. Rodriguez-Aragon, and A. Zhigljavsky, "Singular spectrum analysis for image processing," *Statistics Interface*, vol. 3, no. 3, pp. 419–426, 2010.

[31] H. Devold, *Oil and Gas Production Handbook: An Introduction to Oil and Gas Production*. Morsville, NC, USA: Lulu. Com, 2013.

[32] R. Wan, *Advanced Well Completion Engineering*. Houston, TX, USA: Gulf Professional Publishing, 2011.

[33] E. F. Knott, J. F. Shaeffer, and M. T. Tuley, *Radar Cross Section*, 2nd ed. Raleigh, NC, USA: SciTech, 2004.

[34] A. De Coster and S. Lambot, "Full-wave removal of internal antenna effects and antenna–medium interactions for improved ground-penetrating radar imaging," *IEEE Trans. Geosci. Remote Sens.*, vol. 57, no. 1, pp. 93–103, Jan. 2019.

[35] A. Fawzy, A. Jostingmeier, and A. S. Omar, "Clutter removal for landmine using different signal processing techniques," in *Proc. 10th Int. Conf. Grounds Penetrating Radar*, 2004, pp. 697–700.

[36] S. Navigation, N. S. Route, and G. A. F. Seber, *Multivariate Observations*. Hoboken, NJ, USA: Wiley, 2009.

[37] M. Barkhuizen, "Analysis of process data with singular spectrum methods," Ph.D. dissertation, Univ. Stellenbosch, Stellenbosch, South Africa, 2003.

[38] V. E. Oropeza, "The Singular Spectrum Analysis method and its application to seismic data denoising and reconstruction," M.Sc. thesis, Univ. Alberta, Edmonton, AB, Canada, 2010.

[39] H. Lv *et al.*, "An adaptive-MSSA-based algorithm for detection of trapped victims using UWB Radar," *IEEE Geosci. Remote Sens. Lett.*, vol. 12, no. 9, pp. 1808–1812, Sep. 2015.

[40] N. Golyandina and A. Zhigljavsky, *Singular Spectrum Analysis for Time Series*. New York, NY, USA: Springer, 2013.

[41] N. Golyandina and K. Usevich, "An algebraic view on finite rank in 2D-SSA," in *Proc. 6th St. Petersburg WorkshopSimul.*, 2009, pp. 1–3.

[42] I. Florinsky, *Digital Terrain Analysis in Soil Science and Geology*. New York, NY, USA: Academic, 2016.

[43] N. Golyandina, I. Florinsky, and K. Usevich, "Filtering of digital terrain models by 2D singular spectrum analysis," *Int. J. Ecol. Develop.*, vol. 8, no. F07, pp. 81–94, 2007.

[44] H. Hu, S. Guo, R. Liu, and P. Wang, "An adaptive singular spectrum analysis method for extracting brain rhythms of electroencephalography," *PeerJ*, vol. 5, 2017, Art. no. e3474.

[45] N. Golyandina and K. D. Usevich, "2D-extension of Singular Spectrum Analysis: algorithm and elements of theory," in *Matrix Methods Theory, Algorithms Applications*. Singapore: World Scientific, 2004, pp. 449–473.

[46] S. S. Fayazi, H. S. Lui, and J. Yang, "Microwave imaging of near-field object using ultra-wideband synthetic aperture radar algorithm," in *Proc. IEEE Int. Symp. Antennas Propag.*, 2012, pp. 1–2.

[47] Z. Li, L. Kong, Y. Jia, Z. Zhao, and F. Lan, "A novel approach of multi-path suppression based on sub-aperture imaging in through-wall-radar imaging," in *Proc. IEEE Radar Conf.*, 2013, pp. 1–4.

[48] A. Toktas, E. Yigit, K. Sabanci, and A. Kayabasi, "CFAR based morphological filter design to remove clutter from GB-SAR images: An application to real data," *Microw. Opt. Technol. Lett.*, vol. 59, no. 10, pp. 2685–2692, 2017.

[49] X. Zhuge and A. G. Yarovoy, "A sparse aperture MIMO-SAR-based UWB imaging system for concealed weapon detection," *IEEE Trans. Geosci. Remote Sens.*, vol. 49, no. 1, pp. 509–518, Jan. 2011.

[50] D. M. Sheen, D. L. McMakin, and T. E. Hall, "Three-dimensional millimeter-wave imaging for concealed weapon detection," *IEEE Trans. Microw. Theory Techn.*, vol. 49, no. 9, pp. 1581–1592, Sep. 2001.

[51] X. Zhuge and A. G. Yarovoy, "Three-dimensional near-field MIMO array imaging using range migration techniques," *IEEE Trans. Image Process.*, vol. 21, no. 6, pp. 3026–3033, Jun. 2012.

[52] R. K. Amineh, M. Ravan, A. Khalatpour, and N. K. Nikolova, "Three-dimensional near-field microwave holography using reflected and transmitted signals," *IEEE Trans. Antennas Propag.*, vol. 59, no. 12, pp. 4777–4789, Dec. 2011.

[53] R. K. Amineh, J. J. McCombe, A. Khalatpour, and N. K. Nikolova, "Microwave holography using point-spread functions measured with calibration objects," *IEEE Trans. Instrum. Meas.*, vol. 64, no. 2, pp. 403–417, Feb. 2015.

[54] F. J. Alonso and D. R. Salgado, "Analysis of the structure of vibration signals for tool wear detection," *Mech. Syst. Signal Process.*, vol. 22, no. 3, pp. 735–748, 2008.

[55] D. Oloumi, "Oil well monitoring by ultra-wideband ground penetrating synthetic aperture radar," M.Sc. thesis, Dept. Elect. Eng., Blekinge Institute of Technology, Karlskrona, Sweden, 2012.

[56] SH-3100, Ilmsens GMBH, [Online]. Available: https://www.ilmsens.com/products/mexplore/

[57] J. Sachs *et al.*, "Ultra-wideband pseudo-noise sensors and their application in medical engineering, non-destructive testing and for search and rescue," in *Proc. Internationales Wissenschaftliches Kolloquim*, Ilmenau, Germany, 2009. [Online]. Available: https://www.db-thueringen.de/receive/dbt_mods_00014398

Alireza Akbarpour received the B.S. degree in electrical engineering from Yazd University, Yazd, Iran, in 2013, and the M. S. degree in communication engineering from K. N. Toosi University of Technology, Tehran, Iran, in 2015. He is currently working toward the Ph.D. degree in K. N. Toosi University of Technology.

His research interests include imaging, positioning, and spectroscopy with focus on sensor, antenna, and signal processing

Somayyeh Chamaani (Member, IEEE) received the Ph.D. degree in communications engineering from K. N. Toosi University of Technology, Tehan, Iran, in 2011.

She is currently a Faculty Member of Communications and Bioengineering Groups, K. N. Toosi University of Technology, Tehran, Iran. Since 2017, she has been with the Technische Universität Ilmenau, Ilmenau, Germany, as an experienced Researcher Fellow from the Alexander von Humboldt Foundation. Her research interests include sensing in biomedical and civil applications using ultra-wideband (UWB) technology, including imaging, identification, and localization. In addition to measurement and signal processing of UWB systems, she has contributions in passive UWB components, such as antennas and filters.

Juergen Sachs received the Dr.-Ing degree in surface acoustic devices for solid-state electronics from Technische Universität Ilmenau, Ilmenau, Germany, in 1980.

He was a Senior Lecturer with Technische Universität Ilmenau, Ilmenau, Germany. He taught "Basics of Electrical Measurement Technology," "Measurements in Communications," and "Ultra-Wideband Radar Sensing." He is currently with Ilmsens GmbH, Ilmenau. He was the Head of several research projects, and inter alia coordinator of European projects for humanitarian demining and disaster relief. His research interests include RF-signal analysis and RF-system identification; surface penetrating radar for nondestructive testing and medical engineering, ultra wideband methods and their application in high-resolution radar and impedance spectroscopy, digital processing of ultrawideband signals, array processing; and design and implementation of new RF device approaches.

Giovanni Del Galdo (Member, IEEE) received the Laurea degree in telecommunications engineering from the Politecnico di Milano, Milan, Italy, and the Dr.-Ing. degree on MIMO channel modeling for mobile communications from Technische Universität Ilmenau, Ilmenau, Germany, in 2007.

He then joined the Fraunhofer Institute for Integrated Circuits IIS, Erlangen, Germany, focusing on audio watermarking and parametric representations of spatial sound. Since 2012, he has been leading a joint research group composed of a Department at Fraunhofer Institute for Integrated Circuits IIS, Erlangen, Germany, and, as a Full Professor, a Chair with Technische Universität Ilmenau on the research area of electronic measurements and signal processing. His current research interests include the analysis, modeling, and manipulation of multidimensional signals, over-the-air testing for terrestrial and satellite communication systems, and sparsity promoting reconstruction methods.